ROYAL SOCIETY OF CHEMISTRY

EDGE ARTICLE

Check for updates

A solid dual-salt plastic crystal electrolyte enabling rapid ion transfer and stable interphases for high-performance solid-state sodium ion batteries

Yang Jiang,[a] Rui Wang,[a] Peng Xiong,[a] Yangyang Liu,[a] Hongbao Li,[a] Longhai Zhang,*[a] Ya You [b] and Chaofeng Zhang [*a]

As promising next-generation energy storage systems, solid-state sodium ion batteries (SIBs) are hindered by the low ionic conductivity of their solid electrolytes and poor interfacial compatibility. Here, we developed a solid dual-salt plastic crystal electrolyte (PCE) composed of succinonitrile (SN), fluoroethylene carbonate (FEC), and dual salts ($NaClO_4$ and $NaBF_4$). The synergistic redox reactions of FEC and BF_4^- form a robust, F- and B-rich interphase at electrode/electrolyte interfaces, which significantly enhances interfacial stability and minimizes side reactions that cause cell degradation. Meanwhile, the derived interphase combined with SN's intrinsic oxidation stability endows the PCE with high-voltage tolerance ($\geq$4.75 V), enabling stable operation with high-voltage cathodes. Furthermore, SN's high polarity and plastic character facilitate Na-salt dissociation and optimize interfacial contact, while the competitive coordination of BF_4^- with Na^+ over ClO_4^- increases the free Na^+ concentration, synergistically enhancing ionic conductivity to 3.79 mS cm^{-1}. Consequently, the dual-salt PCE enables high-performance SIBs when paired with multiple electrode materials such as $Na_3V_4(PO_4)_3$, Prussian white, $Na_3V_2(PO_4)_2F_3$ cathodes, and hard carbon anodes. These batteries deliver exceptional cycling stability (over 2500 cycles), rate performance (up to 60C), specific capacity (163.9 mAh g^{-1}), and operating voltage ($\geq$4.0 V). Moreover, the hard carbon$\|Na_3V_4(PO_4)_3$ full cell maintains stable cycling at 10C over 100 cycles, highlighting its promise for practical applications.

1. Introduction

As a promising alternative to lithium-ion batteries (LIBs), sodium-ion batteries (SIBs) are highly competitive due to the high natural abundance and low cost of sodium.[1–4] However, the traditional liquid electrolytes (*e.g.* carbonate- and ether-based) commonly used in SIBs always suffer from inherent drawbacks including leakage, volatility, and flammability, which raise serious safety risks.[5–8] Solid-state electrolytes (SSEs) offer a promising solution with their inherent safety features and potential for higher energy density. Nevertheless, the practical applications of SSEs are still challenged by their low ionic conductivity, high interfacial resistance, and undesirable interfacial side reactions, which result in unsatisfactory battery performance.[9,10] Therefore, the development of advanced SSEs that enable efficient and stable operation in SIBs remains a significant challenge.[11,12]

The plastic crystal electrolyte (PCE) is a novel solid-state electrolyte composed of a metal salt and a plastic crystal. These systems are known for their strong solvation capability and fast ionic transport behaviors. Among various plastic crystals, succinonitrile (SN, NC–CH$_2$–CH$_2$–CN) stands out as a highly polar non-ionic plastic crystal molecule. It maintains a plastic crystalline phase between −40 and 60 °C, which allows it to remain in a solid state and exhibit high safety at room temperature.[13–15] Furthermore, its high polarity and high dielectric constant ($\varepsilon \approx$ 55) promote salt dissociation and support a high concentration of charge carriers. These enable SN-based PCEs to achieve high ionic conductivities of $\approx 10^{-3}$ S cm^{-1} even at room temperature, making them highly attractive for solid-state battery applications. Additionally, SN possesses remarkable oxidation resistance, which makes it suitable for high-voltage battery systems.[16–19]

However, the SN molecule suffers from poor reduction stability. In contact with Na metal, the cyano group (−C≡N) inside could catalyze spontaneous polymerization, forming detrimental by-products. This reaction degrades the electrolyte/electrode interface and leads to irreversible interfacial corrosion, severely compromising the cycling lifespan.[20–23] Furthermore, SN typically exhibits insufficient mechanical strength, which is further exacerbated by the plasticizing effect of high-

[a]Institutes of Physical Science and Information Technology, Leibniz International Joint Research Center of Materials Sciences of Anhui Province, Anhui University, Hefei 230601, China. E-mail: cfz@ahu.edu.cn; zlhedu@ahu.edu.cn

[b]State Key Laboratory of Advanced Technology for Materials Synthesis and Processing, Wuhan University of Technology, Wuhan 430070, China

concentration sodium salts. Although PCEs have been utilized as electrode/electrolyte interphase layers or electrolyte additives in SIBs, their widespread practical application in rechargeable sodium-metal systems remains limited. Therefore, to enable practical deployment, PCEs must address three critical challenges including low mechanical strength, poor reduction stability, and side reactions with Na metal.[24,25]

To overcome the poor reduction stability and mechanical strength of SN-based PCEs, this work develops a solid dual-salt PCE film incorporating SN, fluoroethylene carbonate (FEC), a dual-salt system ($NaClO_4$ and $NaBF_4$), and a glass fiber matrix. The synergistic redox reactions of FEC and BF_4^- lead to a robust, borate- and fluoride-rich interphase on both electrode/electrolyte interfaces, which significantly enhances the interfacial stability and minimizes side reactions that cause cell degradation. The derived robust interphase combined with the intrinsic oxidation stability of SN further endows the electrolyte with high-voltage tolerance up to 4.75 V, enabling stable operation with high-voltage cathodes. SN's high polarity and plastic character can facilitate Na-salt dissociation and enhance interfacial compatibility, while the competitive coordination of BF_4^- with Na^+ over ClO_4^- increases the free Na^+ concentration, synergistically enhancing the ionic conductivity to 3.79 mS cm^{-1}. The glass fiber matrix as the substrate provides critical mechanical reinforcement. As a result, the Na‖$Na_3V_4(PO_4)_3$ cell with a dual-salt PCE exhibits stable cycling over 2500 cycles and superior rate performance (up to 60C). When paired with a hard carbon anode, the hard carbon‖$Na_3V_4(PO_4)_3$ full cell also maintains exceptional cycling stability over 100 cycles at 10C. Moreover, the dual-salt PCE demonstrates good compatibility with Prussian white and $Na_3V_2(PO_4)_2F_3$ cathodes, delivering a high capacity of 163.9 mAh g^{-1} and an operating voltage over 4.0 V, respectively. This work presents a novel design of PCEs with high interfacial stability and compatibility for high-performance solid-state SIBs.

2. Experimental section

2.1. Preparation of the solid dual-salt PCE

A liquid PCE was first obtained by mixing SN (3.6 g, Aladdin), $NaClO_4$ (0.9 g, Aladdin), $NaBF_4$ (0.05 g, Aladdin), and FEC (80 μL, Aladdin) at 65 °C. The resulting liquid PCE was then cast onto a glass fiber (Whatman) reinforcement and allowed to stand for 12 h to complete the solidification process, forming the solid dual-salt PCE. For comparison, the solid $NaClO_4$-PCE and $NaBF_4$-PCE with individual Na salts ($NaClO_4$ or $NaBF_4$) were prepared using the same procedure. All processes of solid PCE preparation were conducted in an Ar-filled glove box (Mikrouna, [O_2] < 0.01 ppm, [H_2O] < 0.01 ppm).

2.2. Preparation of electrodes

In this study, four electrode materials including $Na_3V_4(PO_4)_3$, Prussian white, $Na_3V_2(PO_4)_2F_3$ cathodes, and hard carbon anodes were used to investigate the PCE's compatibility. Among them, $Na_3V_4(PO_4)_3$, $Na_3V_2(PO_4)_2F_3$, and hard carbon were purchased from Guangdong Canrd New Energy Technology Co., Ltd. Prussian white was prepared according to the previously reported

method.[26] Afterward, these electrodes were fabricated by grinding and mixing 65 wt% active material, 5 wt% conductive carbon black, 5 wt% polyvinylidene fluoride (PVDF) binder, and 25 wt% dual-salt plastic crystal in an N-methyl-2-pyrrolidone (NMP) solvent to form a homogeneous slurry. This slurry was then cast onto carbon-coated aluminum foil (Al@C) and finally dried at 50 °C for over 24 h. The NVP active material loading was in the range of 1.2–1.5 mg cm^{-2}, the PW active material loading was in the range of 1–1.2 mg cm^{-2}, the NVPF active material loading was in the range of 1.2–1.4 mg cm^{-2} and the HC active material loading was in the range of 1.1–1.3 mg cm^{-2}.

2.3. Material characterization

PCEs were observed using an optical microscope (YM710TR, Yuescope) and a cryogenic scanning electron microscope (Cryo-SEM, HITACHI Regulus8100). Fourier transform infrared (FTIR, Thermo Fisher Nicolet is5) spectroscopy was performed at ambient temperature. Raman spectra were observed by using a Renishaw inVia-Reflex instrument. Deep etching X-ray photoelectron spectroscopy (XPS, ESCALAB 250Xi) analysis was conducted using an instrument on the surface of the cycled $Na_3V_4(PO_4)_3$ cathode and sodium metal anode.

2.4. Electrochemical measurements

All CR-2032 type coin cells were assembled in a glove box (Mikrouna) and then tested using a PARSTATMC electrochemical workstation (PMC1000) and NEWARE tester (5 V/10 mA, Shenzhen, China). Among them, linear sweep voltammetry (LSV) of the PCE was performed using a stainless steel‖Na cell at 0.1 mV s^{-1}. The corresponding ionic conductivity (σ) and Arrhenius activation energy (E_a) were conducted at different temperatures through electrochemical impedance spectroscopy (EIS) and calculated using the following equation:

$$\sigma = L/RS$$

where L represents the separator thickness and R and S are the bulk resistance and electrode area, respectively.

$$R_{ct}^{-1} = Ae^{-E_a/RT}$$

where R_{ct} stands for the interface resistance, and A, R, and T denote the frequency factor, gas constant, and absolute temperature, respectively. The frequency range of the EIS test is from 10 to 10^5.

The Na^+ transference number (t_{Na^+}) of the PCE was tested according to the chronoamperometry measurement and calculated using the formula

$$t_{Na^+} = I_S(\Delta V - I_0R_0)/I_0(\Delta V - I_SR_S)$$

where I_0, I_S, R_0, and R_S stand for the current and resistance before and after polarization. ΔV corresponds to the applied polarization voltage (10 mV).

The galvanostatic charge/discharge profiles, cycling performance, and rate capability of the assembled cells were determined on a NEWARE tester.

In addition, for the assembly of pouch cells, the NVP cathode (5 × 5 cm), glass fiber (Whatman, GF/A), and the dual-salt PCE were used as the working electrode, separator, and electrolyte, respectively. Subsequently, hard carbon (HC) was used as the anode (5 × 5 cm) for HC//NVP pouch cells.

2.5. Theoretical calculations

The Gaussian 16 program was employed to calculate the highest occupied molecular orbitals (HOMOs), lowest unoccupied molecular orbitals (LUMOs), electrostatic potential (ESP), and binding energy of the various molecular models based on the B3LYP functional method and 6-311+G(b,p) basis set.

3. Results and discussion

We selected SN and $NaClO_4$ as basic solid-state PCEs due to their high ionic conductivity and superior interfacial compatibility. Meanwhile, FEC and $NaBF_4$ were introduced as interfacial film-forming additives to minimize the reactivity of SN toward Na metal and reinforce the PCE's oxidation stability, contributing to stable cycling and higher voltage operation in SIBs. Therefore, a solid dual-salt PCE composed of SN, FEC, $NaClO_4$, and $NaBF_4$ was developed, as shown in Fig. 1a and b. For comparison, solid-state PCEs with individual Na salts ($NaClO_4$ or $NaBF_4$) were prepared to highlight the advantages of the dual-salt system. It should be noted that the poor mechanical strength of solid-state dual-salt PCEs limits their processability and practical application. To address this, a glass fiber (GF) separator was employed as the mechanical reinforcing framework, and the melted dual-salt PCE was poured and re-solidified inside, resulting in a GF supported solid dual-salt PCE film. The optical photographs confirm the successful solidification and uniform filler distribution (Fig. 1c and d). Cross-section cryogenic scanning electron microscopy (Cryo-
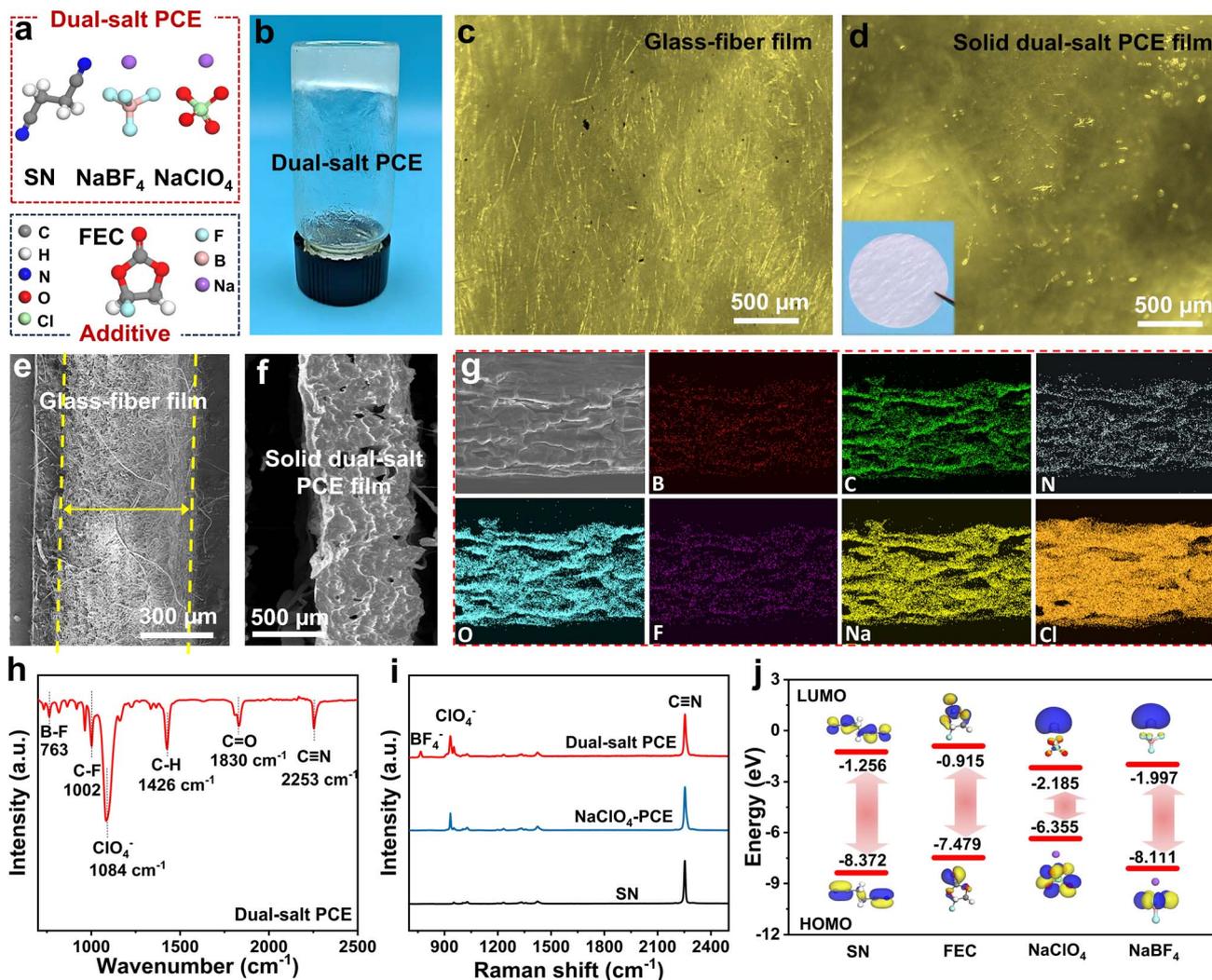

Fig. 1 (a) Schematic illustration of the dual-salt PCE design. (b) The optical photograph of the solid dual-salt PCE. (c and d) The optical photograph of GFs and the GF supported solid dual-salt PCE film. (e and f) Cryo-SEM images of GFs and the GF supported solid dual-salt PCE film. (g) Elemental mapping of the solid dual-salt PCE film. (h) FTIR of the dual-salt PCE. (i) Raman spectra of the dual-salt PCE, $NaClO_4$-PCE, and SN. (j) LUMO and HOMO values of SN, FEC, $NaClO_4$, and $NaBF_4$.

SEM) further verified the filled microstructure and the film thickness of ≈ 0.5 mm (Fig. 1e and f). Afterward, energy-dispersive X-ray spectroscopy (EDS) mapping revealed a homogeneous distribution of the key elements (Na, C, O, N, F, Cl, and B) throughout the film (Fig. 1g), indicating the uniform integration of SN, FEC, $NaClO_4$, and $NaBF_4$. Fourier transform infrared spectroscopy (FT-IR) and Raman spectroscopy further validated this, as shown in Fig. 1h and i. The distinct peaks of $C\equiv N$ (2253 cm^{-1}), $C=O$ (1830 cm^{-1}), C–F (1002 cm^{-1}), ClO_4^- (1084 cm^{-1}), and B–F (763 cm^{-1}) were observed, which originate from SN, FEC, $NaClO_4$, and $NaBF_4$.[27] Meanwhile, the Raman spectra exhibited the characteristic peaks of $C\equiv N$, ClO_4^-, and BF_4^- as well.[28]

Afterward, the highest occupied molecular orbital (HOMO) and lowest unoccupied molecular orbital (LUMO) energy levels of SN, FEC, $NaClO_4$, and $NaBF_4$ were calculated to compare their oxidation and reduction potential (Fig. 1j). As for the HOMO levels, SN and $NaBF_4$ manifest the energy levels of -8.372 and -8.111 eV, respectively, which are lower than those of FEC (-7.479 eV) and $NaClO_4$ (-6.355 eV), indicating their higher anti-oxidation potential. Additionally, dual-salt systems ($NaClO_4$ and $NaBF_4$) exhibited lower LUMO energy levels (-2.185 and -1.997 eV, respectively) than SN (-1.256 eV) and FEC (-0.915 eV), indicating higher reactivity toward reduction at the Na anode. Therefore, the preferential reduction of dual-salt systems ($NaClO_4$ and $NaBF_4$) forms a protective inorganic-rich solid-electrolyte interphase (SEI) layer, which could shield SN from the Na metal, effectively enhancing SN's reduction stability and mitigating undesirable side reactions.

According to electrochemical impedance spectroscopy (EIS) of PCE with different Na salt systems (dual salts, $NaClO_4$, or

$NaBF_4$) at room temperature (Fig. 2a), the dual-salt PCE exhibits the highest ionic conductivity of 3.79×10^{-3} S cm^{-1}, significantly surpassing those of $NaClO_4$-PCE (1.38×10^{-3} S cm^{-1}) and $NaBF_4$-PCE (0.023×10^{-3} S cm^{-1}). This enhancement could be attributed to the increased number of free Na$^+$ in the dual-salt PCE, where BF_4^- competes with ClO_4^- for Na$^+$ coordination (Fig. S1), effectively disrupting the stable ion-pair structure in the single-salt system and increasing the free Na$^+$ concentration. Subsequently, Arrhenius plots show that the dual-salt PCE has a lower activation energy (E_a, 0.175 eV) than the $NaClO_4$-PCE (0.393 eV), indicating its lower energy barrier for Na$^+$ transport inside (Fig. 2b and S2). Moreover, the dual-salt PCE demonstrates an elevated Na$^+$ transport number of 0.68 (Fig. 2c), exceeding that of $NaClO_4$-PCE (0.54, Fig. 2d). Furthermore, the electrochemical stability window of the dual-salt PCE, $NaClO_4$-PCE, and $NaBF_4$-PCE was analyzed by linear sweep voltammetry (LSV) and electrochemical floating analysis (EFA). As shown in Fig. 2e, the dual-salt PCE and $NaBF_4$-PCE exhibit high oxidation potential exceeding 4.75 and 5.0 V $vs.$ Na$^+$/Na, respectively. In contrast, the $NaClO_4$-PCE without $NaBF_4$ exhibits an oxidation potential starting around 4.6 V $vs.$ Na$^+$/Na. Therefore, the enhanced anti-oxidation potential could be attributed to $NaBF_4$. High oxidative stability is crucial for stable operation of high-voltage cathodes like $Na_3V_2(PO_4)_2F_3$. To verify this, the $Na\|Na_3V_2(PO_4)_2F_3$ battery was charged to 4.8 V, as shown in Fig. 2f. The leakage current at 4.7 V still remains below 20 μA, which is well consistent with the LSV result, further demonstrating the dual-salt PCE's outstanding oxidation stability and high-voltage compatibility.

Apart from the oxidation stability and high-voltage compatibility for the cathode, the impact of the dual-salt PCE on the
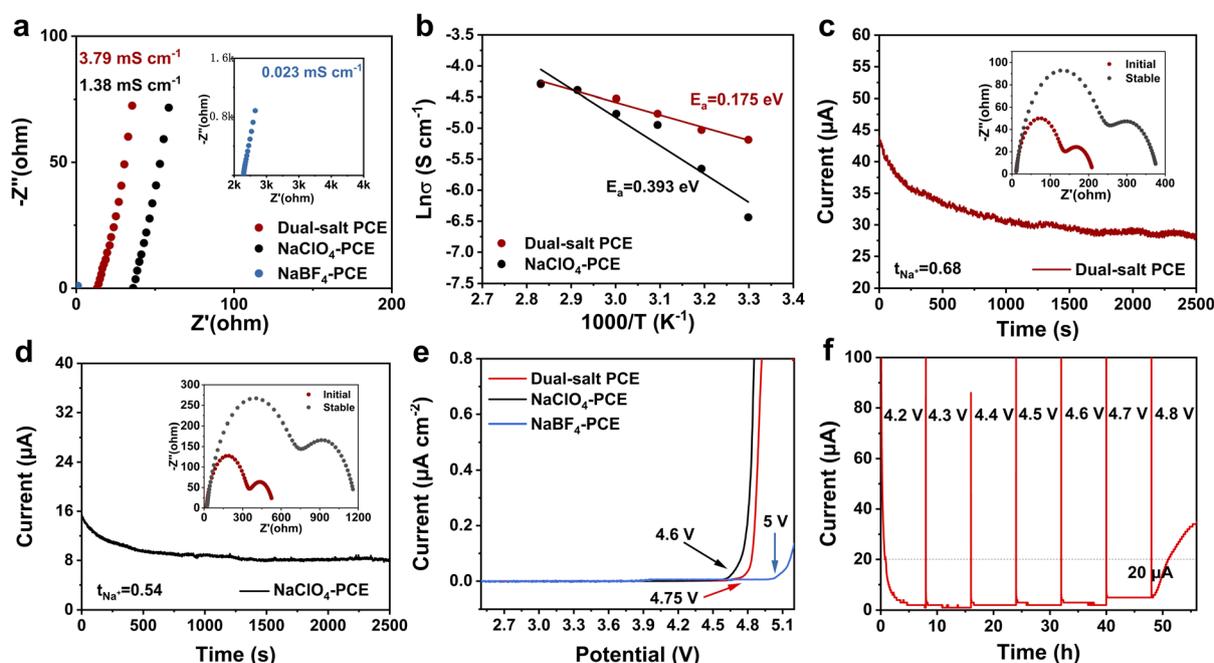

Fig. 2 (a) Ionic conductivity of the dual-salt PCE, $NaClO_4$-PCE, and $NaBF_4$-PCE. (b) Arrhenius plots of the dual-salt PCE and $NaClO_4$-PCE. (c and d) The polarization profiles of the dual-salt PCE and $NaClO_4$-PCE (the insets show the EIS plots before and after polarization). (e) LSV curves of the dual-salt PCE, $NaClO_4$-PCE, and $NaBF_4$-PCE. (f) Electrochemical floating analysis of the dual-salt PCE.
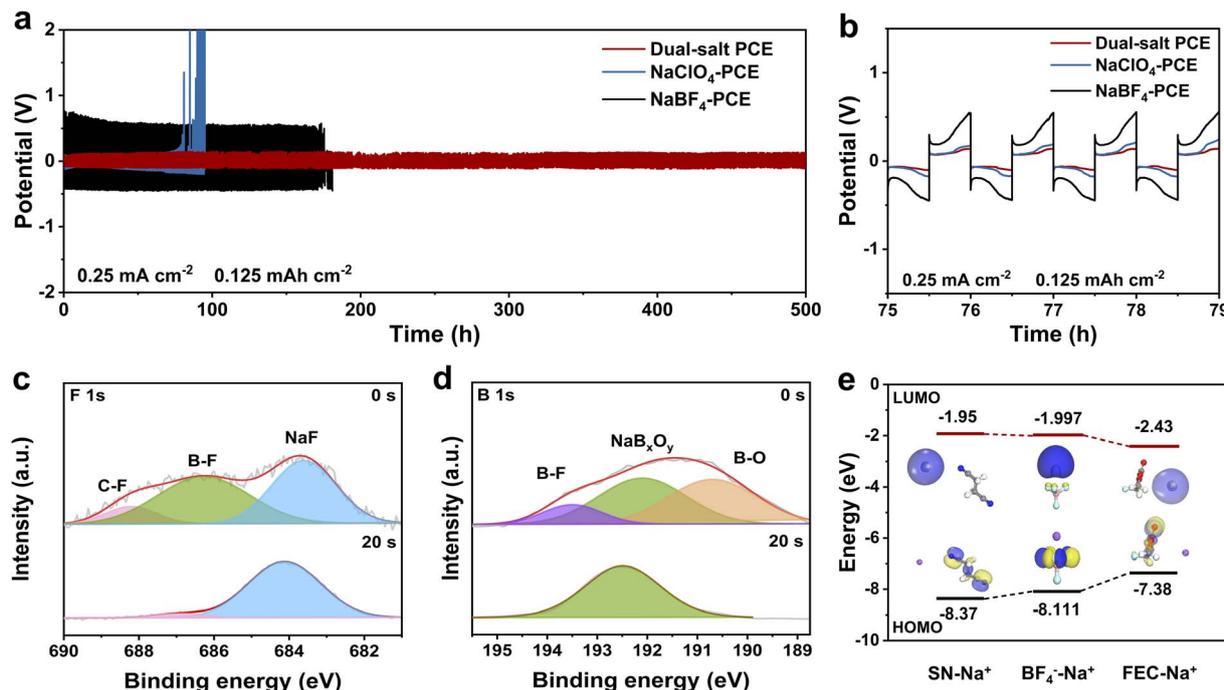
Fig. 3 (a) Voltage profiles of the symmetrical Na‖Na cells with the dual-salt PCE, $NaClO_4$-PCE, and $NaBF_4$-PCE at 0.25 mA cm^{-2}/0.125 mAh cm^{-2}. (b) The enlarged voltage profiles between 75 h and 79 h. XPS depth analysis of (c) F 1s and (d) B 1s for the cycled Na anode in the dual-salt PCE. (e) LUMO/HOMO levels of SN-Na$^+$, BF_4^-- Na$^+$, and FEC-Na$^+$.

stability of the Na metal anode was further investigated. Na symmetrical cells with solid-state PCE films were assembled to evaluate the interfacial behavior between the PCE and Na metal. As displayed in Fig. 3a and b, the Na symmetrical cell can stably cycle over 500 h at 0.25 mA cm^{-2}/0.125 mAh cm^{-2} with a small polarization voltage (Fig. S3), indicating the high compatibility of the dual-salt PCE with Na metal and a stable Na plating/ stripping behavior. In contrast, the cell with $NaClO_4$-PCE fails after only 100 h, accompanied by a continuous increase in polarization. The $NaBF_4$-PCE exhibited a higher overpotential throughout its operation and failed after 200 h. Even at a higher current density of 1 mA cm^{-2} and 0.5 mAh cm^{-2}, the dual-salt PCE still stably cycles for approximately 200 h and exhibits an even and dense surface (Fig. S4).

To investigate the interfacial stability between the dual-salt PCE and Na metal anode, the SEI layer on the cycled Na metal anode was analyzed using deep etching X-ray photoelectron spectroscopy (XPS). As shown in Fig. 3c, the F1s spectrum exhibits a characteristic peak for inorganic NaF at 683.8 eV, which could originate from the decomposition of FEC and BF_4^- anions.[29–31] Owing to its low adsorption energy with SN, NaF serves as a crucial component in the SEI to inhibit side reactions between SN and Na. In addition, the B1s peak was detected and deconvoluted into three peaks corresponding to B–F (193.6 eV), NaB_xO_y (192.2 eV), and B–O (190.7 eV) species (Fig. 3d), confirming the incorporation of both fluorine and boron inside.[32–34] Note that the intensities of the NaF and NaB_xO_y signals both increased and became dominant after sputtering (Fig. 3c and d), while other component signals decreased in the F1s spectrum

(Fig. 3c), indicating the formation of an inorganic-rich, F/B-containing SEI layer. Such a mechanically robust, F/B-rich SEI layer significantly improves the interfacial stability between the dual-salt PCE and Na metal anode. Afterward, the LUMO energy levels of Na$^+$-SN, Na$^+$-FEC, and Na$^+$-BF_4^- were computed to understand the formation of the F/B-containing SEI, as shown in Fig. 3e. Na$^+$-FEC and Na$^+$-BF_4^- both exhibit lower LUMO energies (−2.43 and −1.99 eV, respectively) than that of Na$^+$-SN (−1.95 eV), indicating that FEC and BF_4^- anions are more easily reduced on Na metal to generate NaF- and NaB_xO_y-rich layers, well consistent with the XPS results.

Benefiting from the high ionic conductivity, anti-oxidation/ reduction stability, and comparability of the solid-state dual-salt PCE film, the corresponding Na‖dual-salt PCE‖NVP batteries were expected to exhibit superior performance. As displayed in Fig. 4a and b, the Na‖dual-salt PCE‖NVP cell shows attractive rate capability within the rate range from 1 to 60C. It delivers large discharge capacities of 114.7, 108.5, 104.6, 99.1, 93.1, and 76.6 mAh g^{-1}, respectively. Notably, when the rate returns to 1C, a capacity of 112.9 mAh g^{-1} can be achieved, highlighting its great reversibility. In contrast, Na‖NVP with a liquid electrolyte (LE, 1M $NaClO_4$ in EC : PC = 1 : 1 vol% with 5%FEC) and $NaClO_4$-PCE exhibits poor rate performance especially at a higher rate of 60C, and only 33.1 and 50.7 mAh g^{-1} were retained, respectively. Subsequently, the cycling stability of the Na‖dual-salt PCE‖NVP cell was evaluated at 2C. Encouragingly, it retains a capacity as high as 104.7 with 95.1% capacity retention after 100 cycles (Fig. 4c and d). The corresponding charge/discharge profiles further confirm its stability and well-
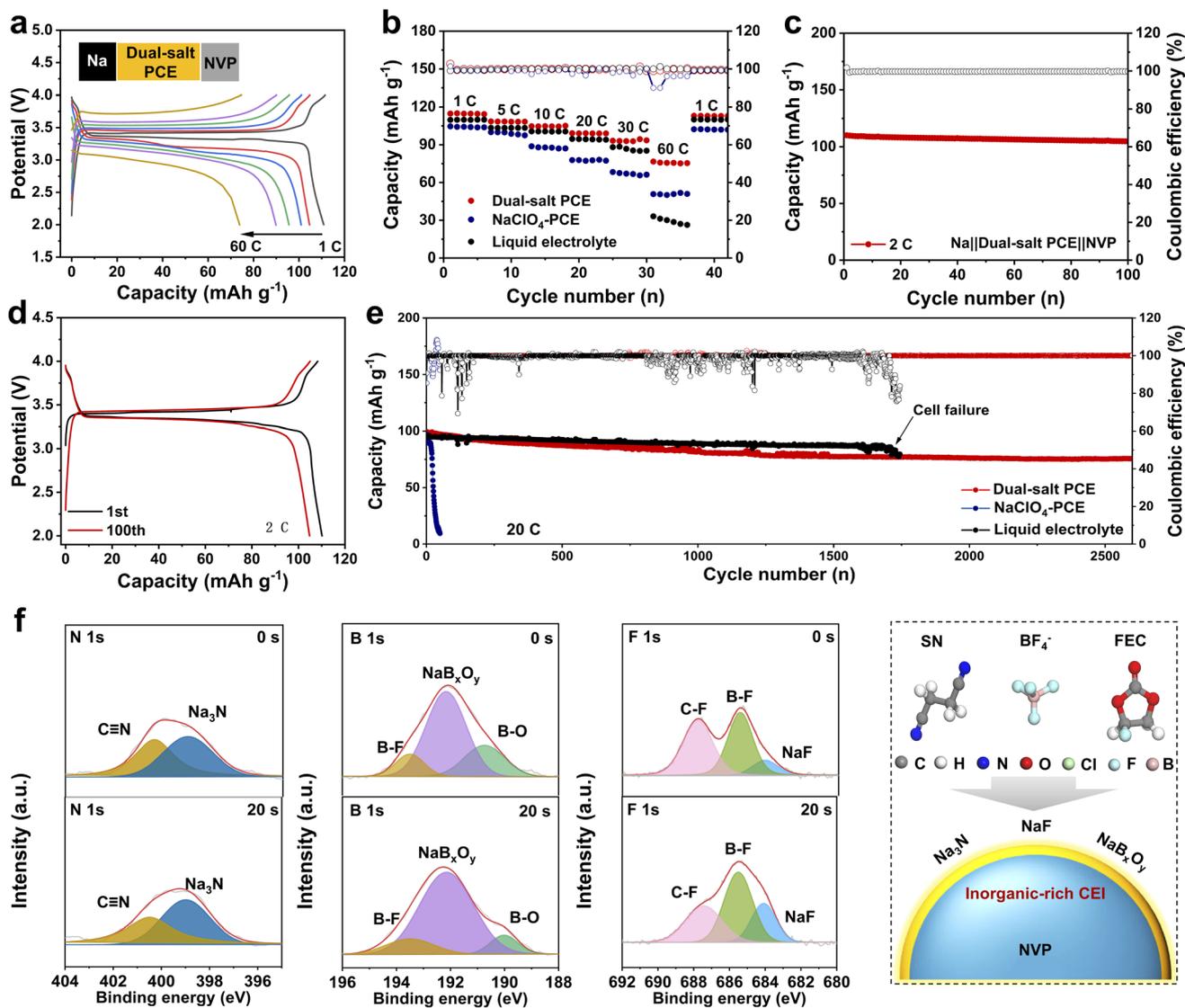
Fig. 4 (a) Charge/discharge profiles of the Na‖NVP cell with the dual-salt PCE at different rates. (b) Rate performance of the Na‖NVP cell with different electrolytes (dual-salt PCE, NaClO$_4$-PCE, and liquid electrolyte). (c and d) Cycling performance and charge/discharge profiles of the Na‖NVP cell at 2C. (e) Long-term cycling performance of the Na‖NVP with different electrolytes at 20C. (f) In-depth XPS spectra of F 1s, N 1s, and B 1s on the cycled NVP cathode in dual-salt PCE. (g) Schematic diagram of the CEI formation.

defined plateaus. Importantly, even at 20C and over 2500 cycles, this battery maintains a capacity of 75.6 mAh g^{-1} (Fig. 4e). In contrast, Na‖NVP cells with LE and NaClO$_4$-PCE fail after 1700 and 20 cycles, respectively. Furthermore, at a rate of 60C, the cell with the dual-salt PCE still cycles stably over 700 cycles (Fig. S5 and S6). To understand the superior stability, we focus on the cathode/electrolyte interface (CEI). Then the CEI formed on the surface of the cycled NVP cathode was analyzed by deep etching XPS. As shown in Fig. 4f and g, the signals for inorganic NaF and NaB$_x$O$_y$ were detected at 684.1 and 192.2 eV before and after sputtering, which are derived from the decomposition of FEC and BF$_4^-$ anions. In addition to NaF and NaB$_x$O$_y$, trace amounts of Na$_3$N (398.9 eV) as a known Na$^+$ conductor were observed on the cathode surface as well (Fig. 4f).[35] This inorganic-rich CEI composed of highly stable NaF/NaB$_x$O$_y$, and

conductive Na$_3$N can be an effective barrier for a stable cathode/electrolyte interface (Fig. 4g).

To evaluate the compatibility and applicability of the solid-state dual-salt PCE, several representative electrodes including Prussian white (PW), Na$_3$V$_2$(PO$_4$)$_2$F$_3$ (NVPF), hard carbon (HC) were investigated. As shown in Fig. 5a, the Na‖PW cell with the solid-state dual-salt PCE delivers a high discharge capacity of 163.9 mAh g^{-1} at 0.1C, accompanied by the typical charge/discharge behaviors of the PW cathode. Notably, even at higher rates of 0.5C and 1C, the cell can stably cycle over 100 cycles and maintain exceptionally high capacities of 142.9 and 126.6 mAh g^{-1}, respectively (Fig. 5b). Additionally, rate capability was further measured at rates from 0.5 to 5C, with capacities of 142.3, 126.6, 109.1, 100.5, and 86.1 mAh g^{-1}, respectively (Fig. 5c and S7). When the rate is returned to 0.5C, the capacity
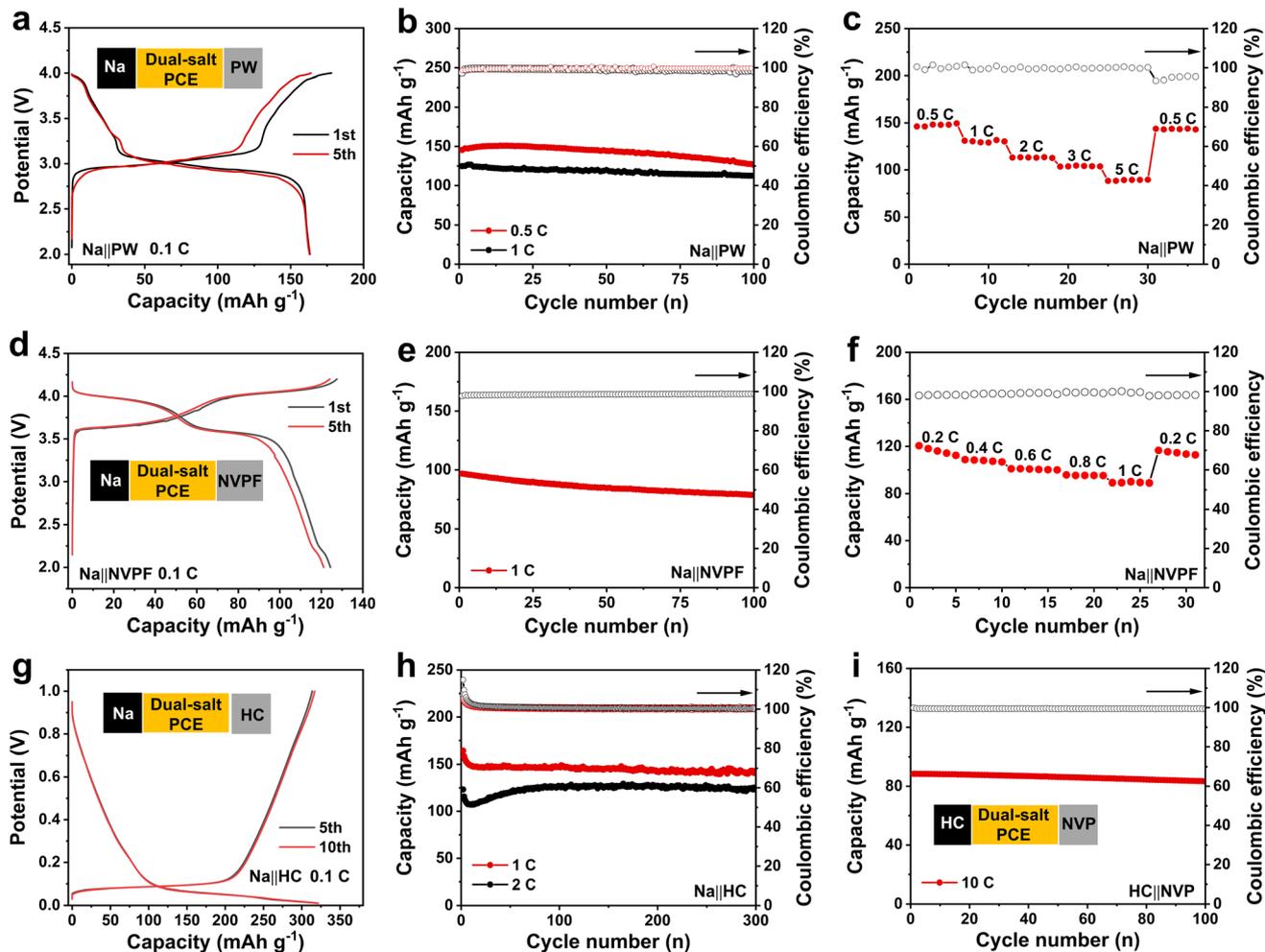
Fig. 5 (a) Charge/discharge profiles of the Na‖dual-salt PCE‖PW cell at 0.1C. (b) Cycling performance of the Na‖dual-salt PCE‖PW cell at 0.5C and 1C, respectively. (c) Rate performance of the Na‖dual-salt PCE‖PW cell. (d) Charge/discharge profiles of the Na‖dual-salt PCE‖NVPF cell at 0.1C. (e) Cycling performance of the Na‖dual-salt PCE‖NVPF cell at 1C. (f) Rate performance of the Na‖dual-salt PCE‖NVPF cell. (g) Charge/discharge profiles of the Na‖dual-salt PCE‖HC cell at 0.1C. (h) Cycling performance of the Na‖dual-salt PCE‖HC cell at 1C and 2C, respectively. (i) Cycling performance of the HC‖dual-salt PCE‖NVP full cell at 10C.

recovers to 142 mAh g^{-1}, highlighting remarkable reversibility. Even paired with a high-voltage NVPF cathode, as displayed in Fig. 5d, the Na‖NVPF cell offers a discharge capacity of 127.5 mAh g^{-1} with an operating voltage over 4.0 V. Meanwhile, the cell presents superior cyclability (89.7 mAh g^{-1} after 100 cycles at 1C) and rate capability (Fig. 5e, f and S8). Beyond cathodes, a hard carbon anode, as a critical component for full cells, was also investigated (Fig. 5g). The Na‖HC cell delivers a discharge capacity of 320.4 mAh g^{-1} at 0.1C along with typical charge/discharge behaviors for hard carbon. Additionally, the cells exhibit stable cycling over 300 cycles at 1C and 2C, maintaining capacities of 146.5 and 124.6 mAh g^{-1}, respectively (Fig. 5h). Afterward, to access practical applications of solid-state dual-salt PCEs, a HC‖Na$_3$V$_2$(PO$_4$)$_3$ full cell was assembled. The full cell exhibits exceptional cycling stability at 10C with minimal capacity decay over 100 cycles (Fig. 5i and S9). Additionally, the pouch cell effectively powers a LED lamp even after repeated flattening and folding (Fig. S10).

4. Conclusion

In summary, this work develops a solid dual-salt PCE film incorporating SN, FEC, a dual-salt system (NaClO$_4$ and NaBF$_4$), and a glass fiber matrix. The synergistic redox reactions of FEC and BF$_4^-$ lead to a robust, borate- and fluoride-rich interphase on both electrode/electrolyte interfaces, which significantly enhances the interfacial stability and minimizes side reactions that cause cell degradation. The derived robust interphase combined with the intrinsic oxidation stability of SN further endows the electrolyte with high-voltage tolerance up to 4.75 V, enabling stable operation with high-voltage cathodes. SN's high polarity and plastic character can facilitate Na-salt dissociation and enhance interfacial compatibility, while the competitive coordination of BF$_4^-$ with Na$^+$ over ClO$_4^-$ increases the free Na$^+$ concentration, synergistically enhancing the ionic conductivity to 3.79 mS cm^{-1}. The glass fiber matrix as the substrate provides critical mechanical reinforcement. Consequently, the

Na‖Na$_3$V$_4$(PO$_4$)$_3$ cell with a solid dual-salt PCE exhibits stable cycling over 2500 cycles and superior rate performance (60C). When coupled with a hard carbon (HC) anode, the HC‖Na$_3$-V$_4$(PO$_4$)$_3$ full cell also delivers stable cycling over 100 cycles at 10C. Moreover, the solid dual-salt PCE demonstrates good compatibility with Prussian white and Na$_3$V$_2$(PO$_4$)$_2$F$_3$ cathodes, both enabling high-performance solid-state SIBs. This work presents a novel design of PCEs with high interfacial stability and compatibility for high-performance solid-state SIBs.

Author contributions

Y. J., L. H. Z., and C. F. Z. designed this work. Y. J., Y. Y. L., and R. W. carried out the synthesis and characterization of the materials. P. X., H. B. L., and Y. Y. performed the data analysis and DFT calculations. Y. Y., L. H. Z., and C. F. Z. co-wrote and supervised the manuscript.

Conflicts of interest

The authors declare no conflict of interest.

Data availability

The data that support the findings of this study are available from the corresponding author upon reasonable request.

Supplementary information (SI): supporting figures including electrochemical performances and SEM characterization. See DOI: https://doi.org/10.1039/d5sc09186a.

Acknowledgements

Notes and references

1 C. Matei Ghimbeu, A. Beda, B. Réty, H. El Marouazi, A. Vizintin, B. Tratnik, L. Simonin, J. Michel, J. Abou-Rjeily and R. Dominko, *Adv. Energy Mater.*, 2024, **14**, 2303833.

2 J. Wang, Y.-F. Zhu, Y. Su, J.-X. Guo, S. Chen, H.-K. Liu, S.-X. Dou, S.-L. Chou and Y. Xiao, *Chem. Soc. Rev.*, 2024, **53**, 4230–4301.

3 Y. Wu, W. Shuang, Y. Wang, F. Chen, S. Tang, X.-L. Wu, Z. Bai, L. Yang and J. Zhang, *Electrochem. Energy Rev.*, 2024, **7**, 17.

4 J. Li, H. Hu, J. Wang and Y. Xiao, *Carbon Neutralization*, 2022, **1**, 96–116.

5 J. Xu, J. Zhang, T. P. Pollard, Q. Li, S. Tan, S. Hou, H. Wan, F. Chen, H. He, E. Hu, K. Xu, X.-Q. Yang, O. Borodin and C. Wang, *Nature*, 2023, **614**, 694–700.

6 Z. Zhang, Y. Li, R. Xu, W. Zhou, Y. Li, S. T. Oyakhire, Y. Wu, J. Xu, H. Wang, Z. Yu, D. T. Boyle, W. Huang, Y. Ye, H. Chen, J. Wan, Z. Bao, W. Chiu and Y. Cui, *Science*, 2022, **375**, 66–70.

7 S. Wan, K. Song, J. Chen, S. Zhao, W. Ma, W. Chen and S. Chen, *J. Am. Chem. Soc.*, 2023, **145**, 21661–21671.

8 Z. Yang, X.-Z. Zhou, Z.-Q. Hao, J. Chen, L. Li, Q. Zhao, W.-H. Lai and S.-L. Chou, *Angew. Chem., Int. Ed.*, 2024, **63**, e202313142.

9 H. Xu, D. Zhang, W. Wang, G. Yu, M. Zhu and Y. Liu, *Carbon Neutralization*, 2025, **4**, e70031.

10 J. Ren, H. Zhu, Y. Fang, W. Li, S. Lan, S. Wei, Z. Yin, Y. Tang, Y. Ren and Q. Liu, *Carbon Neutralization*, 2023, **2**, 339–377.

11 Z. Hu, L. Liu, X. Wang, Q. Zheng, C. Han and W. Li, *Adv. Funct. Mater.*, 2024, **34**, 2313823.

12 J. Wang, D. Yu, X. Sun, H. Wang and J. Li, *eScience*, 2024, **4**, 100252.

13 J.-Y. Hwang, S.-T. Myung and Y.-K. Sun, *Chem. Soc. Rev.*, 2017, **46**, 3529–3614.

14 Z. Lu, H. Yang, Y. Guo, P. He, S. Wu, Q.-H. Yang and H. Zhou, *Angew. Chem., Int. Ed.*, 2022, **61**, e202206340.

15 J. Chen, Z. Yang, X. Xu, Y. Qiao, Z. Zhou, Z. Hao, X. Chen, Y. Liu, X. Wu, X. Zhou, L. Li and S.-L. Chou, *Adv. Mater.*, 2024, **36**, 2400169.

16 S. Zhang, S. Li and Y. Lu, *eScience*, 2021, **1**, 163–177.

17 D. A. Rakov, F. Chen, S. A. Ferdousi, H. Li, T. Pathirana, A. N. Simonov, P. C. Howlett, R. Atkin and M. Forsyth, *Nat. Mater.*, 2020, **19**, 1096–1101.

18 Y. Yan, Z. Liu, T. Wan, W. Li, Z. Qiu, C. Chi, C. Huangfu, G. Wang, B. Qi, Y. Yan, T. Wei and Z. Fan, *Nat. Commun.*, 2023, **14**, 3066.

19 J. Huang, K. Wu, G. Xu, M. Wu, S. Dou and C. Wu, *Chem. Soc. Rev.*, 2023, **52**, 4933–4995.

20 W. Bao, Y. Zhang, L. Cao, Y. Jiang, H. Zhang, N. Zhang, Y. Liu, P. Yan, X. Wang, Y. Liu, H. Li, Y. Zhao and J. Xie, *Adv. Mater.*, 2023, **35**, 2304712.

21 Q. Wang, X. Xu, B. Hong, M. Bai, J. Li, Z. Zhang and Y. Lai, *Chem. Eng. J.*, 2022, **428**, 131331.

22 V. van Laack, F. Langer, A. Hartwig and K. Koschek, *ACS Omega*, 2023, **8**, 9058–9066.

23 J. Ma, M. Yu, M. Huang, Y. Wu, C. Fu, L. Dong, Z. Zhu, L. Zhang, Z. Zhang, X. Feng and H. Xiang, *Small*, 2024, **20**, 2305649.

24 Y. Liu, Y. Zhao, W. Lu, L. Sun, L. Lin, M. Zheng, X. Sun and H. Xie, *Nano Energy*, 2021, **88**, 106205.

25 J. Yu, Y. Zhang, T. Gao, X. Zhang, Y. Lv, Y. Zhang, C. Zhang and W. Liu, *Chem. Eng. J.*, 2024, **487**, 150646.

26 R. Sun and Y. You, *ACS Appl. Mater. Interfaces*, 2023, **15**, 44599–44606.

27 Y. Lu, Y. Cai, Q. Zhang, L. Liu, Z. Niu and J. Chen, *Chem. Sci.*, 2019, **10**, 4306–4312.

28 D. Reber, O. Borodin, M. Becker, D. Rentsch, J. H. Thienenkamp, R. Grissa, W. Zhao, A. Aribia, G. Brunklaus, C. Battaglia and R.-S. Kühnel, *Adv. Funct. Mater.*, 2022, **32**, 2112138.

29 P. Zou, C. Wang, Y. He and H. L. Xin, *Angew. Chem., Int. Ed.*, 2024, **63**, e202319427.

30 F. Feng, Z. Liu, Y. Yan, M. Gong, G. Wang, C. Chi, B. Qi, C. Huangfu, X. Yang, K. Cao, F. Meng, T. Wei and Z. Fan, *Small*, 2024, **20**, 2403275.

31 S. Weng, Y. Liu, S. Lu, J. Xu, J. Xue, H. Tu, Z. Wang, L. Liu, Y. Gao, G. Sun, H. Li and X. Wu, *Angew. Chem., Int. Ed.*, 2025, **64**, e202421602.

32 Z. Yang, J. Pan, H. Wu, K. Shi, Z. Chen, J. Li, W. Huang, T. Yang, Y. Hong, R. Zhang, Z. Lu, J. Li and Q. Liu, *Nano Energy*, 2025, **141**, 111083.

33 L. Gao, J. Chen, Q. Chen and X. Kong, *Sci. Adv.*, 2022, **8**, eabm4606.

34 X. Liu, J. Zhao, H. Dong, L. Zhang, H. Zhang, Y. Gao, X. Zhou, L. Zhang, L. Li, Y. Liu, S. Chou, W. Lai, C. Zhang and S. Chou, *Adv. Funct. Mater.*, 2024, **34**, 2402310.

35 A. Xu, L. Zhao, J. Yu, W. Deng, J. Li, H. Zhang, H. Xu and L. Xu, *Angew. Chem., Int. Ed.*, 2025, **64**, e202506058.